International Journal of Nanomedicine

Dovepress
Taylor & Francis Group

Open Access Full Text Article

ORIGINAL RESEARCH

Dual-Metal Organic Framework Nanozyme for Synergistic Photothermal-Chemodynamic Therapy: Copper-Molybdenum Synergism in Gastric Cancer Treatment

Dachuan Sun[1,2], Bimei Linghu[3], Canrong Lu[1,2], Bo Wei[1,2]

[1]Department of General Surgery, The First Medical Center of Chinese PLA General Hospital, Beijing, 100853, People's Republic of China; [2]Graduate School of Medical School of Chinese PLA Hospital, Beijing, 100853, People's Republic of China; [3]Nankai University, Tianjin, 300071, People's Republic of China

Correspondence: Bo Wei; Canrong Lu, Email weibo@301hospital.com.cn; lucanrong@sohu.com

Purpose: To address the dual challenges of chemotherapy toxicity and poor tumor microenvironment regulation in gastric cancer, we developed a copper-molybdenum bimetallic organic framework nanozyme (CMP) that integrates chemodynamic therapy (CDT) and photothermal therapy (PTT). The system leverages synergistic reactive oxygen species (ROS) generation and localized hyperthermia to deliver efficient, low-toxicity treatment.

Methods: The CMP nanodrug was synthesized by encapsulating Keggin-type phosphomolybdic acid ($H_3PMo_{12}O_{40}$) into copper-based MOF pores via hydrothermal reaction. Physicochemical properties were characterized using transmission electron microscopy (TEM) and X-ray photoelectron spectroscopy (XPS). Systematic evaluation of antitumor efficacy and biosafety was conducted through in vitro assays (CCK-8, calcein-AM/PI staining, ROS detection) and in vivo xenograft models (subcutaneous implantation of NCI-N87 cells in BALB/c nude mice).

Results: The CMP nanozyme demonstrated exceptional photothermal conversion efficiency (29.4% under 808 nm laser). In vitro experiments revealed significant cytotoxicity with ROS elevation. In vivo studies showed significant tumor growth inhibition without hematotoxicity (WBC, ALT levels showed no statistical significance vs. controls). Histopathology confirmed extensive tumor necrosis with preserved cytoarchitecture in vital organs (heart, liver, spleen, and kidney).

Conclusion: The CMP nanozyme achieves potent antitumor efficacy through photothermal-enhanced Fenton-like reactions, depleting glutathione and amplifying ROS. It suppresses gastric cancer in vivo with minimal systemic toxicity, representing a promising nanoplatform for precision therapy.

Keywords: bimetallic organic frameworks, chemodynamic therapy, photothermal therapy, gastric cancer

Introduction

Gastric cancer (GC) is a highly lethal malignancy of the digestive system worldwide, ranking as the fourth most common cancer and the second leading cause of cancer-related mortality.[1] Although advances in surgical techniques, chemotherapy, radiotherapy, and immunotherapy have contributed to reductions in the mortality of GC, the five-year survival rate remains only around 25% or less.[2–5] Additionally, anticancer drugs are limited by the short duration of effective drug concentrations; although increasing the dosage can partially address this limitation, it often leads to severe side effects attributable to drug overdose.[6] In light of these challenges, there is an urgent need to explore novel therapeutic strategies for GC that can overcome the limitations of conventional anticancer drug treatments.

Chemodynamic therapy (CDT) harnesses various transition metal ions to catalyze endogenous hydrogen peroxide (H_2O_2) via Fenton or Fenton-like reactions, thereby generating highly cytotoxic hydroxyl radicals (·OH) capable of eradicating tumor cells. Owing to its remarkable efficacy in treating hypoxic tumors located in deep tissues, coupled with

https://doi.org/10.2147/IJN.S592877
Received: 22 March 2026
Accepted: 15 June 2026
Published: 29 June 2026

minimal damage to healthy tissues, CDT has garnered considerable attention.[7] The ·OH produced during CDT can induce robust immunogenic cell death (ICD), leading to the release of tumor-specific antigens and consequently activating a potent anti-tumor immune response.[8] However, the cytotoxic ·OH may be partially scavenged by the overexpressed glutathione (GSH) present in the tumor microenvironment (TME) prior to exerting its therapeutic effects.[9] In addition, Fe^{2+}-catalyzed CDT—the most prevalent CDT approach—typically requires a highly acidic environment (pH < 4) for activation.[10] Although CDT has exhibited remarkable efficacy in inhibiting tumor growth and metastasis, its ability to completely eradicate tumors remains limited due to the insufficient levels of hydrogen peroxide within the body. Therefore, it is particularly important to combine CDT with other therapeutic modalities and to develop more effective CDT agents. Recent studies showed that copper-based nanomaterials can induce Fenton-like reactions across a broader pH range and demonstrate comparable or even superior performance relative to iron-based nanomaterials.[11,12] Additionally, copper-based nanomaterials possess strong second near-infrared (NIR-II) absorption and excellent photothermal conversion capabilities, offering promising prospects for enhanced catalytic activity and the realization of multimodal therapies combining chemodynamic and photothermal therapy (PTT).[12] This property underscores its significant potential to amplify intracellular oxidative stress within cancer cells.

Photothermal therapy (PTT) exploits photothermal agents capable of absorbing energy from incident light and subsequently converting it into heat, thereby increasing the local temperature of the surrounding environment and inducing tumor cell death.[13,14] PTT not only induces damage to cancer cells but also promotes the generation of reactive oxygen species (ROS) by accelerating the Fenton-like ionization process, thereby achieving a synergistic effect between CDT and PTT.[15] Recently, molybdenum-based nanomaterials (Mo-NMs) have attracted considerable attention as competitive photothermal nanomaterials due to their strong near-infrared (NIR) absorption capacity, high photothermal conversion efficiency (PCE), and favorable biocompatibility.[16] In addition, some Mo-NMs (Mo-POM and Mo-Ox) containing low-valent molybdenum ions ($Mo4^+$ and $Mo3^+$) can react with H_2O_2 in the TME to generate ROS, directly acting as PTT combined CDT agents. It is noteworthy that Mo-POM, as a negatively charged and tunable metal composite nanocluster, can self-assemble into nanostructured aggregates under the mildly acidic conditions present in TME, thereby enhancing their accumulation at tumor sites and activating their NIR photothermal activity and promoting CDT efficacy through the high temperatures generated under PTT.[17–19] Moreover, the reduction of Mo-POM nanoparticles by endogenous GSH permits escape of counteractions from the antioxidant defense system and thus revival of their ability as the CDT/PTT agent, whereby ensuring sustained therapeutic effects for complete cancer elimination.[20]

As an emerging class of porous coordination polymers, metal-organic frameworks (MOFs) have become promising therapeutic platforms owing to their biocompatibility, tunable porosity, endosomal escape capability, and synthetically tailored structures that enable the hierarchical integration of functional entities (eg, nanoparticles and biomolecules) for multifunctionality.[21,22] The integration of MOFs with functional materials has led to the development of advanced multifunctional composites and hybrids, facilitating applications in various cancer therapy modalities, including photodynamic therapy (PDT), photothermal therapy (PTT), chemotherapy, CDT, immunotherapy, and combination therapies.[23–27] For instance, Li et al developed an ORL-loaded copper-based MOF nanodrug (ORL@Cu-MOF) that boosts cuproptosis and suppresses fatty acid metabolism for synergistic therapy of cancer lymph node metastasis.[28] Another study showed that copper-based MOF (Cu-MOF) can kill non-small cell lung cancer cells, especially KRAS-mutant tumors, by simultaneously triggering apoptosis (via copper-induced Fenton reaction and oxidative damage) and cuproptosis (via copper binding to DLAT under FDX1 mediation).[25] Additionally, Bai et al constructed a novel nanozyme, Fe-MOF/CP, based on a cholesterol oxidase-loaded iron-based MOF nanoparticle modified with polyethylene glycol, thereby enabling the synergistic integration of ferroptosis and immunotherapy.[29] Furthermore, Luo et al designed a zinc-ion-doped copper MOF nanocarrier loaded with 5-ALA (5-ALA@Zn-CuTz) for breast cancer therapy; this system selectively targets tumors and inhibits HO-1 expression to enhance PDT efficacy while also providing additional tumor suppression via CDT.[27]

In this study, we loaded Mo-POM into copper-based metal-organic framework (Cu-MOF) to construct a copper-molybdenum bimetallic organic framework nanozyme (CMP). CMP disintegrates in the TME, precisely releases Mo-POM and Cu^{2+}, and converts H_2O_2 into highly toxic · OH, under the 808nm laser irradiation, ultimately integrating

synergistic photothermal-chemodynamic therapy. The system leverages synergistic ROS generation and localized hyperthermia.

Materials and Methods

Materials

Copper(II) nitrate trihydrate ($Cu(NO_3)_2{\cdot}3H_2O$), 1,3,5-benzenetricarboxylic acid (H_3BTC), phosphomolybdic acid ($H_3PMo_{12}O_{40}$), N, N-dimethylformamide (DMF), methylene blue (MB), 5,5-dimethyl-1-pyrroline-N-oxide (DMPO), hydrogen peroxide (H_2O_2, 30%), 5.5′-Dithiobis-2-nitrobenzoic acid (DTNB), and phosphate-buffered saline (PBS) were procured from Beijing Jinglaihuake Biotechnology Co., Ltd. The TMB solution (10 mg/mL in dimethyl sulfoxide) and Calcein AM/PI Double Stain Kit were also supplied by the same vendor. All chemicals were used as received without further purification.

Cell Lines and Animals

Human gastric cancer NCI-N87 (ATCC CRL-5822) was provided by the institution of Biochemistry and Cell Biology, SIBS, CAS (China). NCI-N87 (ATCC CRL-5822) were cultured with RPMI-1640 medium containing 10% fetal bovine serum and 1% penicillin/streptomycin.

BALB/c nude mice (male, 6–8 weeks old, Beijing Viton Lever) were housed in an SPF-grade environment (temperature 22±2°C, humidity 50±10%). All animal experiments were performed in accordance with experimental guidelines approved by the Institutional Animal Care and Use Committee (IACUC) of the Laboratory Animal Center of Jinglai Biology (Approval No.: JLHK-20240601-01.

CMP Nanomedicine System Construction and Multi-Dimensional Characterization

Synthesis of Cu-MOF

Copper(II) nitrate trihydrate ($Cu(NO_3)_2{\cdot}3H_2O$, Sigma-Aldrich, 99.99%), benzene-1,3,5-tricarboxylic acid (H_3BTC, Alfa Aesar, 98%), and N, N-dimethylformamide (DMF, analytical grade) were mixed at a molar ratio of 3:2:200. The mixture was sonicated for 30 min, transferred to a 50 mL PTFE-lined autoclave, and heated at 120°C for 24 h. The resulting blue cubic crystals [$Cu_3(BTC)_2(H_2O)_3$] were purified by three cycles of alternating centrifugation (8,000 rpm, 10 min) in DMF/ethanol, followed by vacuum drying at 60°C for 12 h.

Loading of Molybdenum-Based Polyoxometalate into Cu-MOF to Synthesize CMP

The Cu-MOF precursor (50 mg) was dispersed in an aqueous solution of $H_3PMo_{12}O_{40}$ (10 mg/mL, pH 2.0) and magnetically stirred (600 rpm) for 12 h. POM encapsulation was driven by size-matching effects (MOF pore size: 1.2 nm; Keggin-type POM diameter: 1.0 nm). Unbound POM was removed via centrifugation (10,000 rpm, 15 min), followed by three washes with ultrapure water. The final product (CMP nanoparticles) was obtained by lyophilization (−80°C, 48 h).

Multi-Scale Structural Characterization of CMP

Structural and compositional characterization was performed using advanced analytical techniques. Morphology and elemental distribution were assessed by TEM/HRTEM (JEOL JEM-2100F, 200 kV) with samples dispersed in ethanol and deposited on ultrathin carbon-coated copper grids; EDS mapping (Oxford X-MaxN, 0.1 nm spatial resolution) was used to confirm the dispersion of Cu, Mo, and O throughout the nanostructure. Crystalline phase analysis employed XRD (Bruker D8 Advance, Cu Kα λ=1.5406 Å) at 4° min^{-1} scan rate with 0.02° step size, where diffraction patterns matched JCPDS standards for Cu-MOF (#00-062-1183) and polyoxometallate phases (#00-050-0655). Surface chemistry was investigated by XPS (Thermo Scientific K-Alpha, Al Kα 1486.6 eV), with binding energies referenced to C 1s (284.8 eV), revealing characteristic Cu $2p_3/_2$ (933.5 eV, metallic state) and Mo $3d_5/_2$ (232.8 eV, Mo^{6+}) peaks.

Photothermal Property of CMP

To evaluate the photothermal conversion performance of CMP, the following tests were conducted: temperature variation under irradiation at the same laser power density with different sample concentrations; temperature variation under

irradiation at different laser power densities with the same sample concentration; photothermal conversion stability; and photothermal conversion efficiency. For temperature changes under the same laser power density (808 nm, 1 W cm^{-2}, 10 min) with different sample concentrations, CMP was tested at concentrations of 0.1, 0.2, 0.5, and 1.0 mg/mL. The temperature was recorded every 30s during the 10 min irradiation period. For temperature variation under different laser power densities with the same CMP concentration (1 mg/mL), samples were irradiated for 10 min with an 808 nm laser at power densities of 0.1, 0.2, 0.3, 0.4, and 0.5 W cm^{-2}, and temperature was recorded every 30s using a thermal imager. Photothermal conversion stability was assessed by irradiating a sample at a fixed concentration with a laser power density of 1.0 W cm^{-2} for 2 min, followed by natural cooling to room temperature. This cycle was repeated five times, with temperature recorded every 30s. To determine the photothermal conversion efficiency, the absorbance of CMP nanoparticles at 808 nm was measured at 1.0 mg/mL. The sample was irradiated with a laser power density of 1.0 W cm^{-2} for 10 min until the temperature stabilized, followed by 20 min of natural cooling. Temperature was recorded every 30s throughout the process. The photothermal conversion efficiency was calculated by following the equations:

$$\eta = \frac{[h(ST_{max} - T_{surr}) - Q_{Dis}]}{\left[\left(I1 - 10^{-A}\right)\right]} \times 100\% \quad (1)$$

Here, η refers to the conversion efficiency with an 808 nm laser to heat. T_{Max} is the equilibrium temperature, and T_{Sur} is the ambient temperature. Q_{Dis} is the baseline energy generated by the quartz cell and water upon laser irradiation, which can be calculated independently. I is incident laser power. A is the absorbance of CMP at 808 nm. S is the surface area of the cell, and h is the heat transfer coefficient. hS is calculated from substituting equations:

$$\theta = (\mathrm{T} - T_{surr})/(T_{max} - T_{surr}) \quad (2)$$

θ is the driving force temperature.

$$\mathrm{t} = \tau_s \times (-\ln\theta) \quad (3)$$

t is the time constant in the cooling period.

$$hS = \left(\sum^{m_i} C_{pi}\right)/\tau_s \quad (4)$$

Where m and c are the mass and specific heat capacity of pure water.

ROS Generation of CMP

The generation of ROS by CMP was quantified using electron spin resonance (ESR) spectroscopy. Hydroxyl radical production was detected with DMPO as a spin trapping agent. The reaction mixture consisted of 10 μL of CMP suspension (1 mg/mL), 2 μL of H_2O_2 (100 mM), 10 μL of DMPO (100 mM), and 50 μL of deionized water. After thorough mixing, the sample was immediately transferred into a quartz capillary tube (1.0 mm outer diameter) and analyzed using an ESR spectrometer. For the CMP + laser group, an 808 nm laser (CNI MDL-III-808, 1 W·cm^{-2}) was applied for 5 min prior to measurement. The formation of DMPO/•OH adducts was confirmed by the characteristic 1:2:2:1 quartet signal. Furthermore, •OH generation was also assessed via MB degradation. A total of 50 μL of CMP (1 mg/mL) and 50 μL of H_2O_2 (10 mM) were added to 2 mL of PBS containing MB (20 μg/mL). The decay of the characteristic MB absorption peak at 665 nm was monitored using a UV-Vis spectrophotometer. To evaluate pH dependence, the above experiment was repeated using PBS buffers with different pH values (ranging from 2.0 to 7.4).

GSH Depletion Measurement

To evaluate CMP-induced GSH depletion, a spectrophotometric method based on the reaction between GSH and the specific reagent DTNB was used. In brief, the CMP solution (1 mg/mL) was co-incubated with 1 mM GSH. Subsequently, time points were assessed at 0, 0.5, 1, 2, 3, 4, and 6 hours, and 300 μL of the reaction mixture was added to 1.68 mL of PBS solution (pH 5.5). Next, 20 μL of DTNB solution (0.5 mg/mL in ethanol) was added. GSH depletion was determined by measuring the optical density (OD) at 412 nm using UV-visible spectrophotometry.

Cytotoxicity in vitro NCI-N87 GC Cells

The NCI-N87 GC cell experiment was divided into seven groups (each group n=3), and the treatment methods for each group were as follows: (1) PBS control; (2–4) treatment with CMP at concentrations of 25, 50, and 100 μg/mL; (5–7) treatment with CMP at the same concentrations (25, 50, 100 μg/mL) combined with laser irradiation (808 nm, 1 W/cm^2, 5 minutes).

Cellular viability was assessed using complementary CCK-8 and live/dead staining protocols. For CCK-8 quantification, cells pretreated for 24 hours were seeded in 96-well plates. Following medium aspiration, 10 μL CCK-8 reagent (Dojindo) was added per well, incubated at 37°C/5% CO_2 for 1 h, and absorbance was measured at 450 nm using a BioTek Synergy H4 microplate reader. Viability was calculated as: (OD of the experimental group/OD of the control group) ×100%. Parallel live/dead evaluation utilized cells cultured in 24-well plates. After PBS washing, cells were stained with 250 μL Calcein AM/PI solution (2 μM Calcein AM, 4 μg/mL PI) for 30 min at 37°C (light-protected), then imaged on a Nikon Eclipse Ti fluorescence microscope using appropriate filter sets (green: live cells, Ex/Em=494/517 nm; red: dead cells, Ex/Em=535/617 nm).

Chemodynamic Activities of CMP in NCI-N87 GC Cells

To determine the chemodynamic activity of CMP in NCI-N87 GC cells, following 12-hour experimental group treatments as mentioned above, cells were seeded in 6-well plates. Culture medium was aspirated, and cells were washed twice with PBS (2 mL/well, 5 min/wash). Then, cells were incubated with 10 μM DCFH-DA in serum-free medium (1:1000 dilution, 1 mL/well) at 37°C under 5% CO_2 for 20 min. Then, 6-well plates were taken out, and cells were washed twice with PBS (2 mL/well). Observe the green fluorescence immediately under a fluorescence microscope (Nikon Eclipse Ti) and take pictures. Quantitative analysis was performed by measuring mean fluorescence intensity per field using ImageJ (Fiji distribution).

In vivo Therapeutic Effects and Systemic Toxicity of CMP-Mediated Photothermal-Chemodynamic Therapy

To develop the tumor-bearing mice model, NCI-N87 cells were resuspended at a concentration of 1×10^7 cells/mL in a 1:1 mixture of Matrigel (Corning) and PBS. A total volume of 100 μL of this suspension was injected subcutaneously into the right dorsal flank of each nude mice. When tumor volumes reached approximately 100 ± 10 mm^3 (about 10 days post-inoculation), the mice were randomly allocated into five groups (n=8 per group): G1 (PBS control), G2–G4 (CMP at 25, 50, and 100 mg/kg, respectively), and G5 (CMP 100 mg/kg + Laser irradiation). The sample size (n = 8 per group) for animal experiments was chosen based on previous studies using similar in vivo models and common standards in the field, and was considered sufficient to detect biologically meaningful differences in tumor growth while minimizing animal use, in accordance with the 3Rs principle. Treatments were administered every other day for a total of seven administrations. Tumor dimensions were measured every two days using digital calipers, and the volume was calculated as $V = 0.5 \times L \times W^2$, where L and W represent the longest and shortest diameters, respectively. The tumor growth index (TGI) for each group was determined by comparing tumor volume at certain time points to baseline (start of treatment), allowing for assessment of treatment-induced tumor inhibition.[30] All animals were euthanized 48 hours after the final treatment for terminal analysis. Body weights and excised tumor weights were recorded.

Systemic inflammatory responses and overall toxicity were assessed via sequential biomonitoring. On day 7 of treatment, serum was collected from two mice per group by retro-orbital bleeding (200 μL whole blood centrifuged at 3000 × g for 15 min). The pro-inflammatory cytokines IL-6 and TNF-α were quantified using species-specific ELISA kits.

Terminal evaluations were conducted 48 hours after the final administration. Under anesthesia, 150 μL of whole blood was collected from the retro-orbital plexus into EDTA-coated tubes for complete blood count analysis (Mindray BC-5390; parameters included WBC, lymphocytes, monocytes, and eosinophils). In parallel, 350 μL of blood was centrifuged (3000 × g, 15 min) to obtain serum for biochemical testing on a Hitachi 7180 analyzer (ALT, AST, CREA-S, UA). Following blood collection, mice were euthanized by cervical dislocation.

Major organs (heart, liver, spleen, lungs, and kidneys) were harvested, fixed, and processed for H&E staining (5 min hematoxylin/2 min eosin). Histopathological evaluation was performed in accordance with ISO 10993–6 standards using an Olympus BX53 microscope, enabling a systematic assessment of nanodrug-induced toxicity in normal tissues and organs. Tumor measurements and histological analyses were performed by an investigator blinded to group assignment.

Statistical Analysis and Visualization

Data are presented as mean ± standard deviation (mean ± SD). For accurate analysis of the experimental results, GraphPad Prism 10.0 was used to perform two-tailed Student's t-tests for comparisons between two groups and one-way ANOVA for comparisons among multiple groups. Statistical significance was set at *$p < 0.05$, **$p < 0.01$, ***$p < 0.001$, and ****$p < 0.0001$. Experimental groups followed the principle of random allocation. Each experiment was repeated at least three times ($n \geq 3$) to ensure objectivity and reliability of the results.

Results and Discussion

Characterization of CMP

In this study, CMP nanomedicine consisted of molybdenum-based polyoxometalate and copper-based metal-organic framework. In this nanomedicine, Mo-POM, as a negatively charged and tunable metal composite nanocluster, can self-assemble into nanostructured aggregates under the mildly acidic conditions present in TME, thereby enhancing their accumulation at tumor sites and activating their NIR photothermal activity and promoting CDT efficacy through the high temperatures generated under PTT.[17,18,31] Copper ions (Cu^{2+}) can be reduced to Cu^{+} under a high concentration of L-glutathione in the tumor site to further efficiently trigger the Fenton-like reaction to convert H_2O_2 into highly toxic • OH-mediated CDT.[32,33] In this study, we load molybdenum-based polyoxometalate into a copper-based metal-organic framework to realize their effective delivery to solid tumors for photothermal-chemodynamic synergistic therapy.

Herein, the synthesis and working mechanisms of CMP for combined tumor PTT/CDT therapy are illustrated in Figure 1. CMP nanodrug exhibited a well-defined cubic morphology with uniform dispersion, as evidenced by TEM and SEM imaging (Figure 2A and B). Hydrodynamic diameter analysis indicated a narrow size distribution centered at approximately 100 nm (Figure 2C). Elemental mapping confirmed the homogeneous distribution of Cu and Mo throughout the nanostructure (Figure 2D). XRD and XPS analyses confirm that copper in our nanodrug exists as Cu(II) within the Cu-BTC paddlewheel units of $[Cu_2(BTC)_4/_3(H_2O)_2]_6[H_3PMo_{12}O_{40}]$, as evidenced by the Cu $2p_3/_2$ peak at 933.5 eV and its characteristic satellite features (typical of Cu(II)). Meanwhile, the Mo $3d_5/_2$

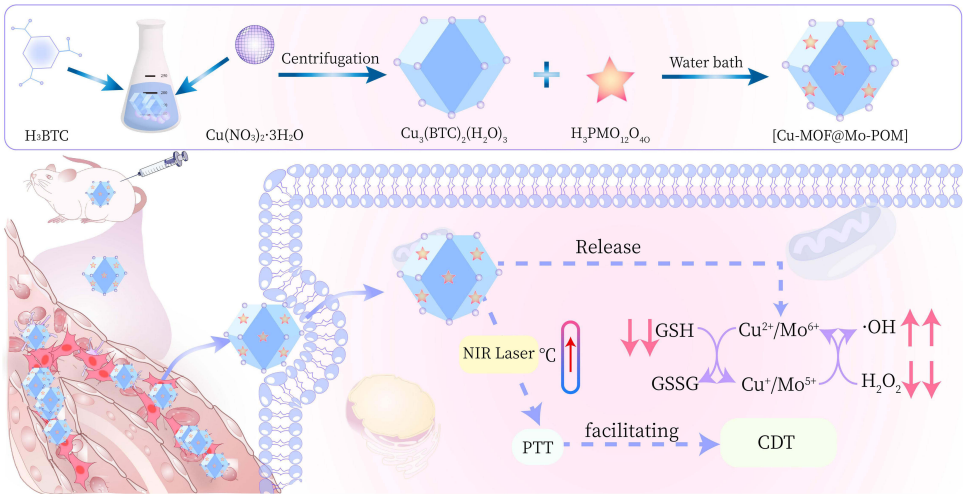

Figure 1 Illustration of synthesis and working mechanisms of CMP for combined tumor PTT/CDT therapy.

https://doi.org/10.2147/IJN.S592877

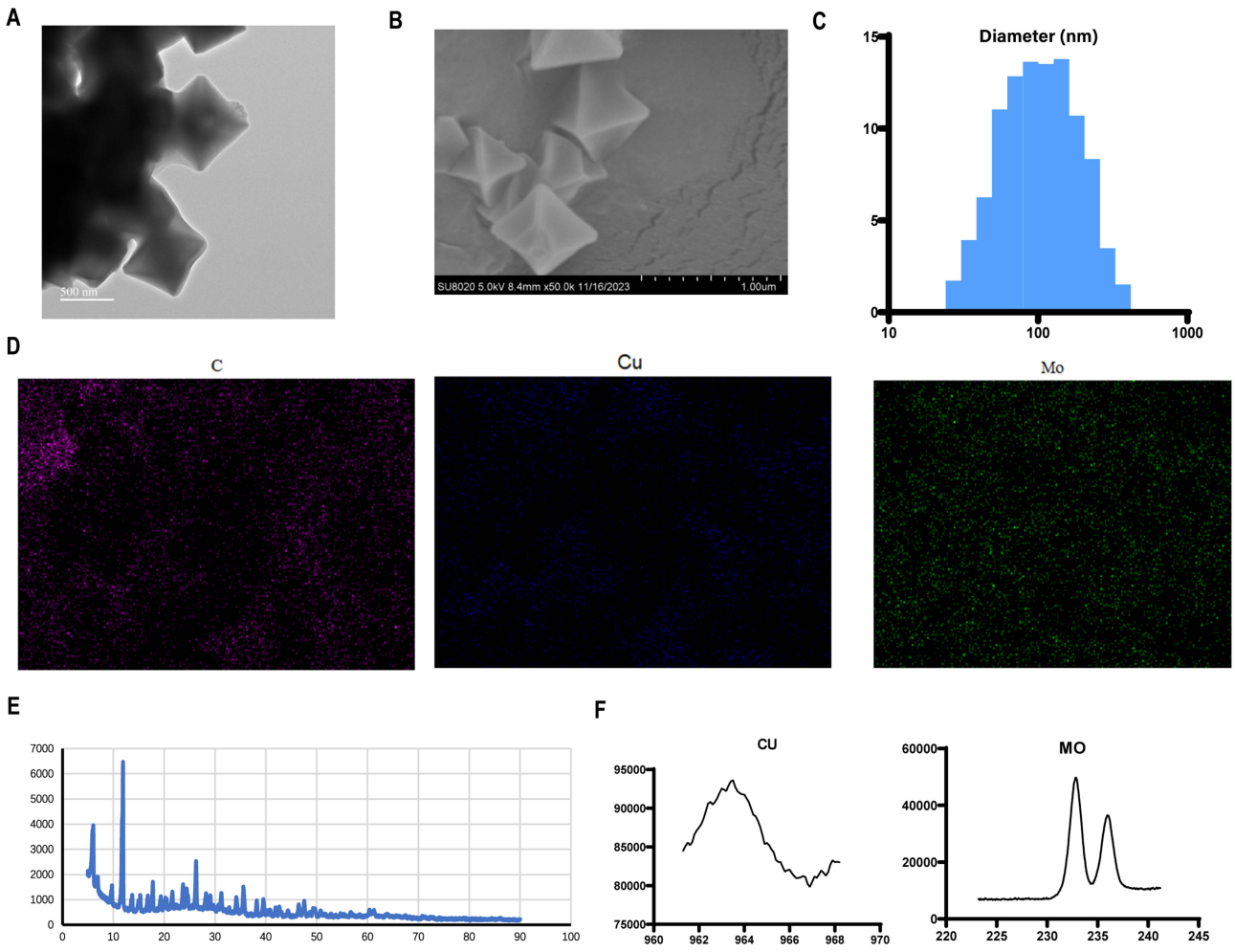

Figure 2 Characterization of CMP. (**A** and **B**) TEM and SEM show that CMP has a cubic morphology with uniform particle size (~100 nm) and good dispersion. (**C**) Hydrodynamic diameter of CMP. (**D**) Elemental mapping of CMP. (**E**) XRD spectra show that CMP successfully integrates the crystalline structural features of Cu-MOF and Keggin-type POM. (**F**) Crystallographic phase analysis- XRD E ICP-MS analysis reveals that the loading of CMP with Cu and Mo is respectively 16.46% and 19.94%.

signal at 232.8 eV is consistent with the Mo^{6+} oxidation state. (Figure 2E and F). Quantitative ICP-MS measurements established a composition of 16.46% Cu and 19.94% Mo per 100 g CMP (Supplementary Table 1). The cubic architecture of CMP provides critical advantages over conventional spherical nanoparticles.

ROS Generation, GSH Depletion, and Photothermal Conversion Efficiency of CMP

Studies have shown that in the presence of elevated GSH levels, copper ions (Cu^{2+}) can be reduced to Cu^{+}, simultaneously oxidizing GSH to glutathione disulfide (GSSG). This reaction depletes intracellular GSH reserves, while the generated Cu^{+} efficiently catalyzes a Fenton-like reaction to convert H_2O_2 into hydroxyl radicals, thereby enabling chemodynamic therapy.[33,34] Similarly, Mo^{4+}/Mo^{5+} ions also function as Fenton-like reagents, producing •OH from H_2O_2. Within the tumor microenvironment, these molybdenum ions are further oxidized to higher valence states (Mo^{5+}/Mo^{6+}), a redox process that concurrently consumes GSH and generates GSSG.[35]

ESR spectroscopy was performed using DMPO as a spin-trapping agent to detect •OH generation. As shown in Figure 3A, the characteristic 1:2:2:1 quartet signal in the ESR spectrum, corresponding to the DMPO-•OH adduct, confirmed the production of a substantial amount of •OH. The generation of •OH under different conditions was further quantified via a •OH-induced methylene blue (MB) degradation assay by monitoring the decrease in absorbance at 665 nm.[36] Under physiological pH conditions (pH 7.4), the temporal decrease in MB absorbance was minimal (Figure 3B), indicating that CMP generates only negligible amounts of ROS in a normal

https://doi.org/10.2147/IJN.S592877

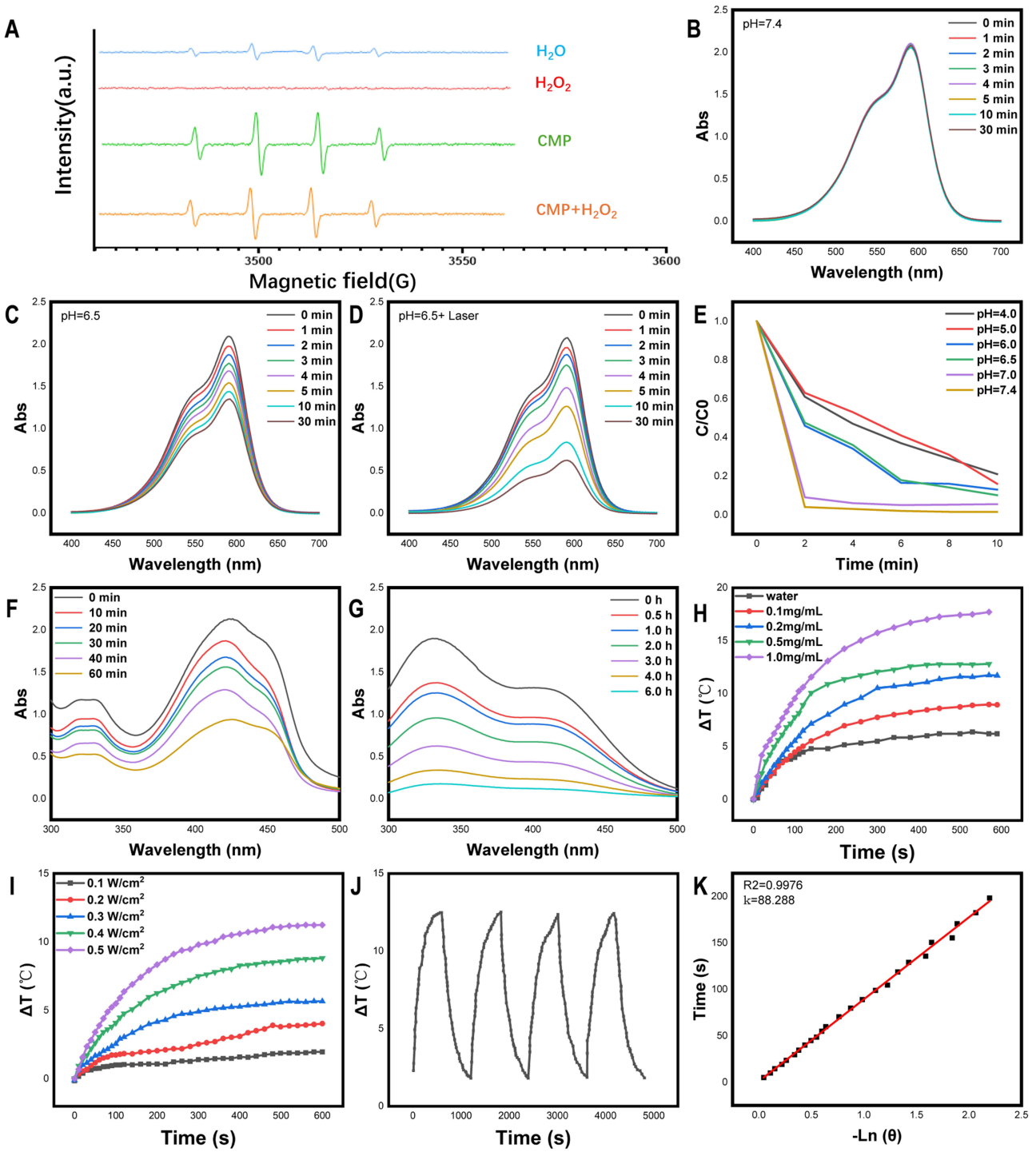

Figure 3 ROS Generation, GSH Depletion, and photothermal conversion efficiency of CMP. (**A**) ESR confirms that CMP significantly catalyzes the generation of hydroxyl radicals (•OH). MB degradation of CMP in (**B**) physiological environment (pH 7.4), (**C**) weakly acidic environment (pH 6.5), (**D**) pH 6.5 with laser irradiation. (**E**) The influence of pH (range 4–7.4) on •OH production of CMP. (**F**) H_2O_2 degradation of CMP. (**G**) GSH depletion of CMP at pH 6.5. (**H**) Temperature changes of CMP with various concentrations upon 808 nm laser irradiation treatment (1 W/cm2). (**I**) Heating curves of CMP (1 mg/mL) under 808 nm laser irradiation treatment with various power densities ranging from 0.1 to 0.5 W/cm2 for 10 min. (**J**) Recycling heating curves of CMP (0.5 mg/mL) with laser (808 nm, 0.5 W/cm2). (**K**) Corresponding cooling time constant (τs) calculation.

https://doi.org/10.2147/IJN.S592877

physiological milieu, which suggests low potential toxicity to normal tissues and favorable biological safety. In contrast, under weakly acidic conditions (pH 6.5), CMP induced a significant reduction in MB absorbance within 30 minutes (Figure 3C), demonstrating its efficient ROS-generating capacity and distinct acid-responsive property in an acidic microenvironment. Notably, when weak acidity was combined with laser irradiation, the decrease in MB absorbance was even more rapid and pronounced (Figure 3D). This finding indicates that the photothermal effect can markedly enhance the copper/molybdenum ion-mediated Fenton-like reactions within CMP, enabling rapid and substantial ROS production under acidic conditions. The pH adaptability of the CMP nanodrug was further evaluated. Impressively, CMP maintained excellent catalytic activity over a wide pH range of 4 to 7 (Figure 3E). The broad pH adaptability of CMP provides a distinct advantage for applications in the tumor microenvironment (TME), especially when compared with traditional Fenton-like catalysts (eg, Fe^{2+} catalyzed chemodynamic therapy), which typically require a highly acidic environment (pH < 4) to function effectively.[37] To further investigate the catalytic mechanism by which CMP decomposes H_2O_2 through Fenton/Fenton-like reactions, we employed the titanium sulfate colorimetric method to detect its H_2O_2 consumption capacity. As shown in Figure 3F, the absorbance at 412 nm decreased significantly within 60 minutes, indicating that CMP possesses excellent H_2O_2 consumption ability. In summary, these results demonstrate that CMP can efficiently generate •OH radicals for CDT via Fenton-like reactions, while laser irradiation can synergistically enhance ROS production.

In addition, we used 5,5′-dithiobis (2-nitrobenzoic acid) (DTNB) to detect the consumption of GSH. DTNB can be reduced by GSH to form a yellow product, which has a characteristic absorption at 412 nm. As shown in Figure 3G, the absorbance at this wavelength decreased significantly over time. This indicates that under acidic conditions, Cu^{2+} and Mo^{6+} released by CMP can rapidly consume GSH, thereby effectively weakening the scavenging effect of high-concentration GSH in tumor cells on ROS and further enhancing the efficacy of CDT.

The photothermal conversion performance of CMP was further systematically evaluated. As shown in Figure 3H, the temperature of the CMP solution increased gradually with rising concentration, demonstrating a clear concentration-dependent photothermal response. At a concentration of 1 mg/mL, the temperature rise reached approximately 17°C, indicating its strong potential for PTT. In contrast, under identical irradiation conditions, pure water exhibited only a marginal temperature change, confirming that the heating effect originated primarily from CMP itself.

Moreover, the photothermal conversion efficiency of CMP was found to be closely related to the laser power density (Figure 3I): higher power densities led to more significant temperature increases. Beyond its excellent photothermal performance, CMP also displayed remarkable photothermal stability. Over five consecutive irradiation cycles, the temperature rise remained nearly consistent, stabilizing at around 12.5°C in each cycle (Figure 3J). Finally, the photothermal conversion efficiency of CMP was calculated to be 29.4% (Figure 3K). The high photothermal conversion efficiency, coupled with outstanding photothermal stability, underscores the considerable potential of CMP for applications in photothermal therapy.

Dose-Dependent Cytotoxicity and ROS Amplification in vitro

Given the intrinsic catalase-like activity and superior photothermal performance of CMP, we further investigated its antitumor effects at the cellular level. To assess the cytotoxic potential of CMP, CCK-8 assays were conducted on NCI-N87 GC cells. The results showed that the cell viability of NCI-N87 cells treated with CMP was significantly lower than that of the control PBS group, and cell viability gradually decreased with increasing concentrations of CMP. Notably, combined treatment with CMP and laser irradiation led to a further reduction in cell viability (Figure 4A). To more intuitively and clearly visualize the antitumor efficacy of CMP, calcein AM/PI double staining was performed on cells from different treatment groups. As shown in Figure 4B and C, CMP treatment induced a concentration-dependent increase in red fluorescence (indicative of PI-positive dead cells). Importantly, the number of live cells (green fluorescence) was further diminished following combined CMP and laser irradiation. To elucidate the underlying cytotoxic mechanism, we evaluated the ROS generation capacity of CMP in NCI-N87 GC cells using the DCFH-DA fluorescent probe. The experimental results indicated that GC cells treated with CMP exhibited significantly higher fluorescence

 https://doi.org/10.2147/IJN.S592877

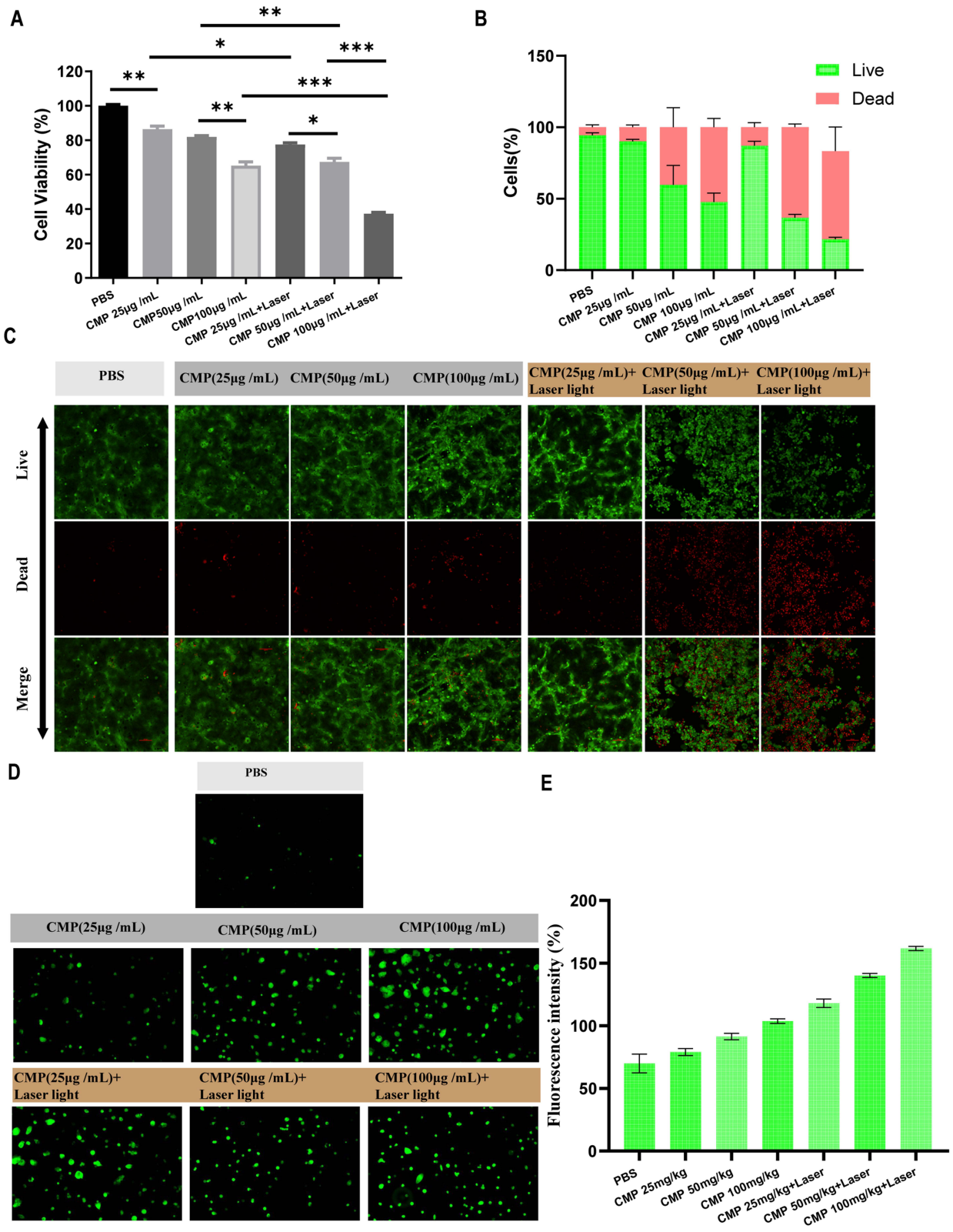

Figure 4 Dose-Dependent Cytotoxicity and ROS Amplification In Vitro. (**A**) CCK-8 results showed that CMP dose-dependently inhibited NCI-N87 cell activity, and further decreased after combined laser irradiation (***p<0.001). (**B** and **C**) Calcein/PI staining and corresponding fluorescence quantitative analysis intensity results. (**D** and **E**) ROS staining and corresponding fluorescence quantitative analysis intensity results. (* $p < 0.05$, ** $p < 0.01$, *** $p < 0.001$, and **** $p < 0.0001$.).

https://doi.org/10.2147/IJN.S592877

intensity compared to the control PBS group, suggesting the substantial generation of •OH in the treatment groups. Furthermore, ROS levels showed a dose-dependent elevation upon CMP treatment. Remarkably, this oxidative stress was further significantly amplified when CMP treatment was combined with laser irradiation (808 nm, 1 W cm^{-2}, 5 min), as quantified by DCF fluorescence intensity (Figure 4D and E). The results directly demonstrate that the synergistic cytotoxicity observed with CMP plus laser irradiation is mechanistically driven by the massive generation of cytotoxic ROS via PTT-enhanced CDT. Collectively, these in vitro findings strongly confirm the intrinsic tumoricidal efficacy of CMP and underscore the superior therapeutic outcome achievable through the combination of photothermal-enhanced CDT (PTT/CDT).

The potential PTT - CDT synergistic mechanism of CMP may arise from three interdependent processes: (1) Photothermal Priming & Reaction Acceleration: CMP efficiently absorbs NIR light (808 nm) and converts it into localized heat. This thermal energy not only directly damages cells but critically accelerates the Fenton-like reaction kinetics involving the Cu species within CMP, thereby dramatically promoting the catalytic decomposition of H_2O_2 into highly cytotoxic hydroxyl radicals. (2) Thermo-Catalytic Feedback Enhancement: The elevated local temperature profoundly enhances the electron transfer kinetics between Cu^+/Cu^{2+} redox pairs. This orders-of-magnitude acceleration under photothermal conditions massively boosts •OH yield from available H_2O_2. (3) Antioxidant Defense Disruption (Glutathione Depletion): Upon release into the TME, Cu^{2+} can deplete excessively expressed endogenous GSH, subsequently converting into the more potent Cu^+, the produced Cu+ ions form a closed-loop for continuous generation of hydroxyl radical and singlet oxygen with H_2O_2 as substrates.[38,39] Concurrently, the Mo^{6+} components in CMP actively deplete the key cellular antioxidant GSH by oxidizing it to its disulfide form (GSSG).[35] This targeted depletion cripples the cell's primary defense mechanism against ROS, preventing the scavenging of the generated •OH and other radicals, and allowing oxidative stress to reach lethal levels. This triad of mechanisms—photothermal acceleration of catalysis, thermal enhancement of reaction kinetics, and targeted disabling of antioxidant defenses—acts concertedly to create a self-reinforcing cycle of oxidative damage. The heat from PTT accelerates radical production (1,2), while Cu^{2+}/Mo^{6+}-mediated GSH depletion (3) prevents their neutralization. This ensures the Fenton-like reaction proceeds unchecked at an amplified rate, resulting in an overwhelming and sustained flux of cytotoxic free radicals, primarily •OH, that drives the observed synergistic cell death. This sophisticated multi-mechanistic synergy positions CMP as a highly effective agent for combined PTT/CDT, maximizing ROS-mediated tumor cell killing while leveraging the unique properties of its composite structure.

In vivo Tumor Suppression and Systemic Toxicity Assessment

Building upon the promising in vitro tumoricidal efficacy of CMP, we proceeded to evaluate its in vivo antitumor potential using an ectopic GC mice model, with concurrent assessment of systemic biosafety. The therapeutic efficacy of the CMP-mediated CDT/PTT combination therapy on tumor growth was evaluated in a mice model bearing NCI-N87 human GC xenografts. When tumor volume reached approximately 100 mm^3, the mice were respectively administered PBS, CMP (25 mg/kg), CMP (50 mg/kg), CMP (100 mg/kg), or CMP (100 mg/kg) plus laser irradiation every other day for a total of seven times treatments. Tumor growth and body weight changes were monitored throughout the treatment period.

Throughout the dosing period, only minor fluctuations in body weight were observed across all groups, with no significant reduction in any treatment group (Figure 5A), indicating that none of the administered regimens induced substantial systemic toxicity. Tumor volume was further monitored to evaluate the in vivo antitumor efficacy. In the PBS group, tumor volume continued to increase over time. By contrast, CMP treatment suppressed tumor growth in a dose-dependent manner, and the antitumor effect was significantly enhanced in the CMP + Laser group (Figure 5B), consistent with cellular-level observations and supporting a synergistic PTT/CDT effect. The therapeutic outcome was also assessed using the tumor growth inhibition (TGI) value, calculated as the ratio of the final tumor volume to the volume at the first treatment. Compared with the PBS group (TGI = 5.42 ± 3.27), the CMP100mg/kg + Laser group showed a markedly lower TGI (0.34 ± 0.12), confirming the potent tumor-suppressive effect of CMP-mediated PTT/CDT (Figure 5C). This result was corroborated by terminal relative

 https://doi.org/10.2147/IJN.S592877

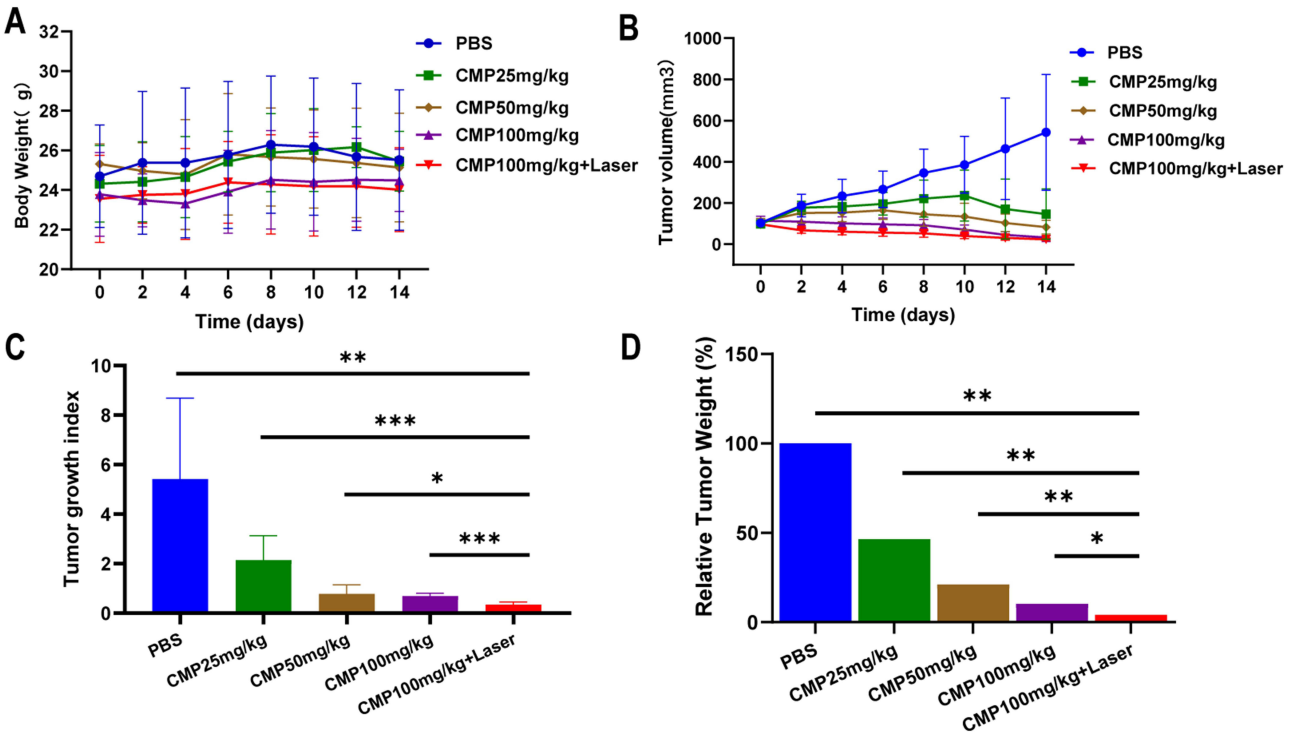

Figure 5 In Vivo Tumor Suppression and Systemic Toxicity Assessment. (**A**) The mice's body weight, (**B**) tumor volume, (**C**) tumor growth index, and (**D**) relative tumor weight recordings for each group. (* $p < 0.05$, ** $p < 0.01$, *** $p < 0.001$, and **** $p < 0.0001$.).

tumor weight measurements across groups (Figure 5D). The strong in vivo antitumor activity confirms the successful translation of CMP's in vitro performance to a complex biological system.

The systemic toxicity of combined tumor PTT/ CDT therapy strategies was further investigated. Throughout the dosing period, serum cytokine profiling revealed no elevation of key pro-inflammatory markers IL-6 or TNF-α (Figure 6A), effectively ruling out concerns over CMP-induced systemic inflammatory responses—a key advantage for clinical translation. Routine hematological and biochemical analyses showed that levels of WBC, lymphocytes, monocytes, and eosinophils, ALT, AST, CREA-S, and UA in all treated mice remained within normal ranges and showed no significant differences compared with the control group (Figure 6B and C). Furthermore, H&E staining of major organs (heart, liver, spleen, lungs, and kidneys) revealed no obvious pathological abnormalities in any treatment group, including PBS, CMP alone, and CMP + Laser (Figure 6D).

Collectively, these results demonstrate the favorable biosafety profile of the CMP-based nanomedicine. The CMP exhibits significant antitumor efficacy in vivo while maintaining low systemic toxicity, as evidenced by potent dose-dependent tumor growth inhibition and the absence of notable hematological toxicity, organ damage, or systemic inflammation. These results provide compelling preclinical support for the clinical translation of CMP and establish a solid foundation for exploring its broader application in tumor therapy, particularly through the combined photo-thermal-enhanced CDT mechanism identified in vitro.

Although these preclinical results are promising, several limitations exist in this study. First, this study uses only a subcutaneous xenograft model. Future studies should incorporate orthotopic and patient-derived xenograft (PDX) models to better recapitulate the tumor microenvironment. Additionally, long-term (>60 days) follow-up and chronic toxicity assessment are lacking. While our results indicate ROS-mediated tumor inhibition, the proposed redox cycle and the detailed synergistic mechanism require further validation using techniques such as electron spin resonance (ESR), specific ROS scavengers, and direct measurements of Cu^{+}/Cu^{2+} or Mo species changes. These limitations must be addressed before clinical consideration.

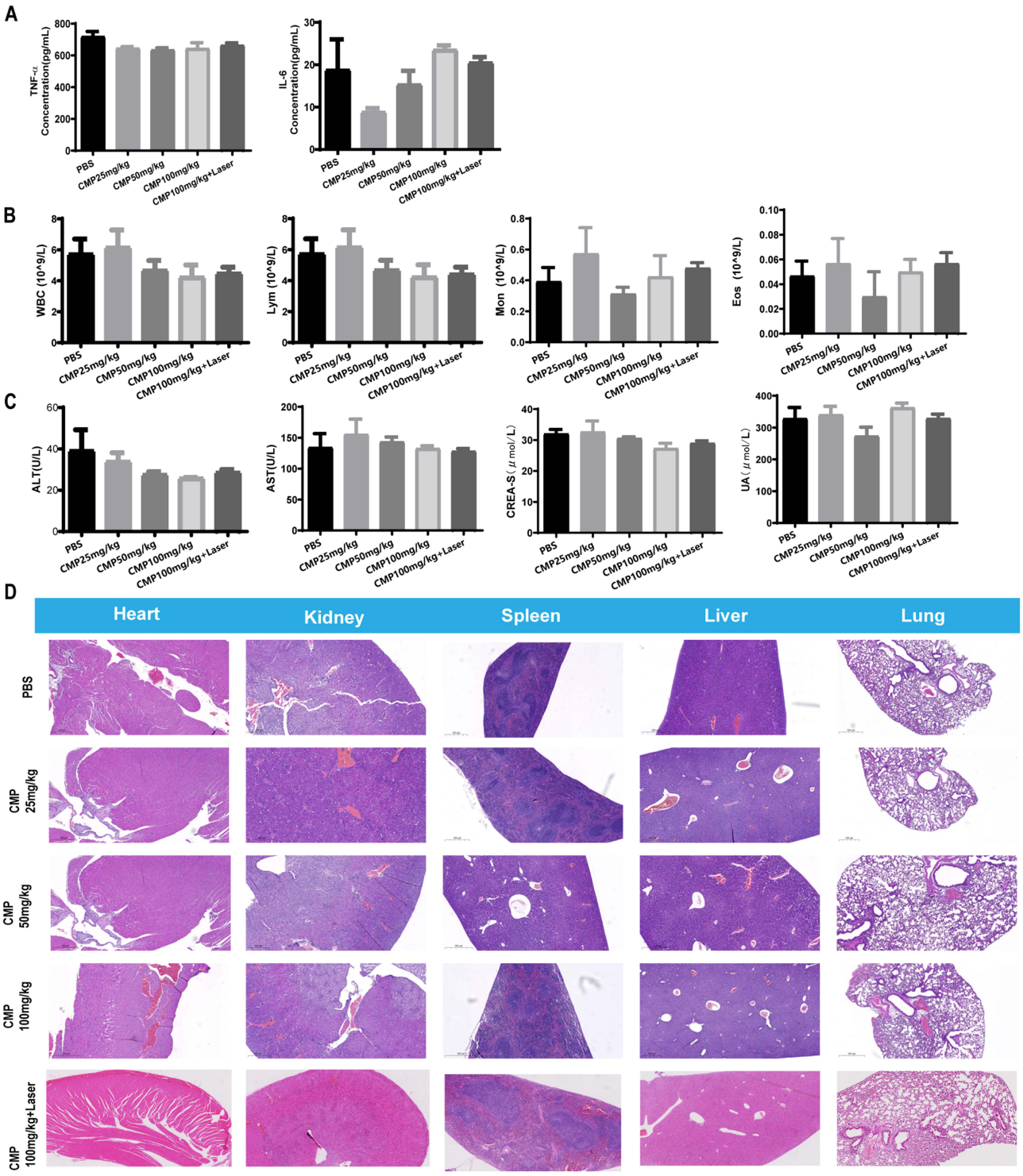

Figure 6 Systemic Toxicity Assessment. (**A**) ELISA results of IL-6 and TNFα. (**B**) Blood routine results of WBC, Lymphocytes, Monocytes, and Eosinophils. (**C**) Blood biochemistry results of ALT, AST, CREA-S, and UA. (**D**) H&E staining results of major organs (heart, liver, spleen, lungs, and kidneys).

Conclusion

In summary, we successfully constructed a copper-molybdenum bimetallic nanozyme (CMP) with tumor microenvironment responsiveness. CMP exhibits excellent photothermal conversion efficiency (29.4%) and robust Fenton-like activity. Under acidic conditions and laser irradiation, CMP generates massive hydroxyl radicals, depletes glutathione,

https://doi.org/10.2147/IJN.S592877

and amplifies oxidative stress in gastric cancer cells. In vivo studies confirm that CMP significantly suppresses tumor growth in a dose-dependent manner without causing systemic toxicity, hematological abnormalities, or organ damage. The favorable biosafety profile and potent antitumor efficacy position CMP as a promising nanoplatform for precision cancer therapy, meriting further clinical translation research.

Data Sharing Statement

Data yielded in our study will be made available by the authors to any qualified researchers.

Ethics Approval and Consent to Participate

The animal study protocol was reviewed and approved by the Institutional Animal Care and Use Committee (IACUC) of the Laboratory Animal Center of Jinglai Biology (Approval No.: JLHK-20240601-01). All animal experiments were performed in strict accordance with the approved guidelines, and all efforts were made to minimize animal suffering and reduce the number of animals used. All in vitro experiments were performed using commercially available, well-characterized cell lines (e.g., Human gastric cancer NCI-N87 (ATCC CRL-5822)) that were purchased from Biochemistry and Cell Biology, SIBS, CAS (China). This study involved no human participants, tissue samples, or patient data, so written informed consent was not required. All procedures complied with the Declaration of Helsinki and institutional ethics.

Author Contributions

All authors made a significant contribution to the work reported, whether that is in the conception, study design, execution, acquisition of data, analysis and interpretation, or in all these areas; took part in drafting, revising or critically reviewing the article; gave final approval of the version to be published; have agreed on the journal to which the article has been submitted; and agree to be accountable for all aspects of the work.

Funding

This study was supported by Beijing Natural Science Foundation (No.7232149), the National Natural Science Foundation of China (No.82073192, No.82572862, No.62133010), and the Beijing Science and Technology Program (No. Z221100007422125).

Disclosure

The author(s) report no conflicts of interest in this work.

References

1. Sung H, Ferlay J, Siegel RL, et al. Global cancer statistics 2020: GLOBOCAN estimates of incidence and mortality worldwide for 36 cancers in 185 countries. *CA Cancer J Clin*. 2021;71(3):209–249. doi:10.3322/caac.21660
2. Cats A, Jansen EPM, van Grieken NCT, et al. Chemotherapy versus chemoradiotherapy after surgery and preoperative chemotherapy for resectable gastric cancer (CRITICS): an international, open-label, randomised Phase 3 trial. *Lancet Oncol*. 2018;19(5):616–628. doi:10.1016/S1470-2045(18)30132-3
3. de Steur WO, van Amelsfoort RM, Hartgrink HH, et al. Adjuvant chemotherapy is superior to chemoradiation after D2 surgery for gastric cancer in the per-protocol analysis of the randomized CRITICS trial. *Ann Oncol off J Eur Soc Med Oncol*. 2021;32(3):360–367. doi:10.1016/j.annonc.2020.11.004
4. van der Kaaij RT, Koemans WJ, van Putten M, et al. A population-based study on intestinal and diffuse type adenocarcinoma of the oesophagus and stomach in the Netherlands between 1989 and 2015. *Eur J Cancer Oxf Engl*. 2020;130:23–31. doi:10.1016/j.ejca.2020.02.017
5. Zhang L, Liu X, Lin H, Wang J, Zhang Q. [Factors affecting survival prognosis of advanced gastric cancer and establishment of a nomogram predictive model]. *Nan Fang Yi Ke Da Xue Xue Bao*. 2021;41(4):621–627. Chinese. doi:10.12122/j.issn.1673-4254.2021.04.21
6. Kyu Shim M, Yang S, Sun IC, Kim K. Tumor-activated carrier-free prodrug nanoparticles for targeted cancer Immunotherapy: preclinical evidence for safe and effective drug delivery. *Adv Drug Deliv Rev*. 2022;183:114177. doi:10.1016/j.addr.2022.114177
7. Tang Z, Liu Y, He M, Bu W. Chemodynamic therapy: tumour microenvironment-mediated Fenton and Fenton-like reactions. *Angew Chem Int Ed Engl*. 2019;58(4):946–956. doi:10.1002/anie.201805664
8. Zhou H, Bao P, Lin YT, et al. Bimetallic nanoreactor mediates cascade amplification of oxidative stress for complementary chemodynamic-immunotherapy of tumor. *Biomaterials*. 2025;317:123075. doi:10.1016/j.biomaterials.2024.123075
9. Lin LS, Song J, Song L, et al. Simultaneous Fenton-like ion delivery and glutathione depletion by MnO2 -based nanoagent to enhance chemodynamic therapy. *Angew Chem Int Ed Engl*. 2018;57(18):4902–4906. doi:10.1002/anie.201712027

10. Bian Y, Liu B, Ding B, et al. Tumor microenvironment-activated nanocomposite for self-amplifying chemodynamic/starvation therapy enhanced IDO-blockade tumor immunotherapy. *Adv Sci*. 2023;10(34):e2303580. doi:10.1002/advs.202303580
11. Su Z, Li J, Zhang D, Ye P, Li H, Yan Y. Novel flexible Fenton-like catalyst: unique CuO nanowires arrays on copper mesh with high efficiency across a wide pH range. *Sci Total Environ*. 2019;647:587–596. doi:10.1016/j.scitotenv.2018.08.022
12. Hu R, Fang Y, Huo M, et al. Ultrasmall Cu2-xS nanodots as photothermal-enhanced Fenton nanocatalysts for synergistic tumor therapy at NIR-II biowindow. *Biomaterials*. 2019;206:101–114. doi:10.1016/j.biomaterials.2019.03.014
13. Overchuk M, Weersink RA, Wilson BC, Zheng G. Photodynamic and photothermal therapies: synergy opportunities for nanomedicine. *ACS Nano*. 2023;17(9):7979–8003. doi:10.1021/acsnano.3c00891
14. Xie B, Xiao Z, Ling J, Peng Y, Chen T. Exploring the application of metal-based photothermal agents in photothermal therapy combined with immune checkpoint therapy. *Front Pharmacol*. 2025;16:1553158. doi:10.3389/fphar.2025.1553158
15. Qian X, Zhang J, Gu Z, Chen Y. Nanocatalysts-augmented Fenton chemical reaction for nanocatalytic tumor therapy. *Biomaterials*. 2019;211:1–13. doi:10.1016/j.biomaterials.2019.04.023
16. Zhou Z, Li X, Hu T, et al. Molybdenum-based nanomaterials for photothermal cancer therapy. *Adv NanoBiomed Res*. 2022;2(11):2200065. doi:10.1002/anbr.202200065
17. Chen C, Mao S, Tan C, et al. General synthesis of ordered mesoporous carbonaceous hybrid nanostructures with molecularly dispersed polyoxometallates. *Angew Chem Int Ed Engl*. 2021;60(28):15556–15562. doi:10.1002/anie.202104028
18. Ni D, Jiang D, Valdovinos HF, et al. Bioresponsive polyoxometalate cluster for redox-activated photoacoustic imaging-guided photothermal cancer therapy. *Nano Lett*. 2017;17(5):3282–3289. doi:10.1021/acs.nanolett.7b00995
19. Shi G, Jiang H, Yang F, et al. NIR-responsive molybdenum (Mo)-based nanoclusters enhance ROS scavenging for osteoarthritis therapy. *Pharmacol Res*. 2023;192:106768. doi:10.1016/j.phrs.2023.106768
20. Liu G, Zhu J, Guo H, et al. Mo2 C-derived polyoxometalate for NIR-II photoacoustic imaging-guided chemodynamic/photothermal synergistic therapy. *Angew Chem Int Ed Engl*. 2019;58(51):18641–18646. doi:10.1002/anie.201910815
21. Du J, Li F, Sun L. Metal-organic frameworks and their derivatives as electrocatalysts for the oxygen evolution reaction. *Chem Soc Rev*. 2021;50 (4):2663–2695. doi:10.1039/d0cs01191f
22. Liu J, Huang J, Zhang L, Lei J. Multifunctional metal-organic framework heterostructures for enhanced cancer therapy. *Chem Soc Rev*. 2021;50 (2):1188–1218. doi:10.1039/d0cs00178c
23. Chahal S, Babu A, Vasukutty A, Park IK. Bioorthogonal Cu-MOF nanocatalyst enables GSH-triggered in situ drug synthesis for xCT-driven ferroptosis in colorectal cancer. *J Control Release off J Control Release Soc*. 2026;393:114775. doi:10.1016/j.jconrel.2026.114775
24. Chen K, Zhou A, Zhou X, He J, Xu Y, Ning X. Cellular Trojan Horse initiates bimetallic Fe-Cu MOF-mediated synergistic cuproptosis and ferroptosis against malignancies. *Sci Adv*. 2024;10(15):eadk3201. doi:10.1126/sciadv.adk3201
25. Li K, Wu L, Wang H, et al. Apoptosis and cuproptosis co-activated Copper-based metal-organic frameworks for cancer therapy. *J Nanobiotechnology*. 2024;22(1):546. doi:10.1186/s12951-024-02828-3
26. Guo Z, Xiao Y, Wu W, et al. Metal-organic framework-based smart stimuli-responsive drug delivery systems for cancer therapy: advances, challenges, and future perspectives. *J Nanobiotechnology*. 2025;23(1):157. doi:10.1186/s12951-025-03252-x
27. Luo X, Qi H, Yan M, et al. Multifunctional nanoplatform for tumor chemodynamic and self-amplified photodynamic cascade therapy. *J Adv Res*. 2026;79:721–736. doi:10.1016/j.jare.2025.03.056
28. Li ZZ, Liu Y, Zhou K, et al. ORL@Cu-MOF Boost cuproptosis and suppress fatty acid metabolism for cancer lymph node metastasis synergistic therapy. *Adv Sci*. 2025;12(35):e02154. doi:10.1002/advs.202502154
29. Bai T, Xue P, Shao S, Yan S, Zeng X. Cholesterol depletion-enhanced ferroptosis and immunotherapy via engineered nanozyme. *Adv Sci*. 2024;11 (38):e2405826. doi:10.1002/advs.202405826
30. Sun R, Zhang Y, Lin X, et al. Aminopeptidase N-responsive conjugates with tunable charge-reversal properties for highly efficient tumor accumulation and penetration. *Angew Chem Int Ed Engl*. 2023;62(9):e202217408. doi:10.1002/anie.202217408
31. Zhang C, Bu W, Ni D, et al. A polyoxometalate cluster paradigm with self-adaptive electronic structure for acidity/reducibility-specific photothermal conversion. *J Am Chem Soc*. 2016;138(26):8156–8164. doi:10.1021/jacs.6b03375
32. Zuo W, Fan Z, Chen L, et al. Copper-based theranostic nanocatalysts for synergetic photothermal-chemodynamic therapy. *Acta Biomater*. 2022;147:258–269. doi:10.1016/j.actbio.2022.05.030
33. Hao YN, Zhang WX, Gao YR, Wei YN, Shu Y, Wang JH. State-of-the-art advances of copper-based nanostructures in the enhancement of chemodynamic therapy. *J Mater Chem B*. 2021;9(2):250–266. doi:10.1039/d0tb02360d
34. Bao Y, Zhang H, Wu X, et al. Dual-Responsive Cu(I) and Cu(II) Co-doped carbon dots for synergistic chemodynamic-photothermal antitumor therapy. *ACS Appl Nano Mater*. 2023;6(15):14410–14420. doi:10.1021/acsanm.3c02418
35. Zhang P, Bai H, Yao Z, et al. Tumor microenvironment responsive chitosan-coated W-doped MoOx biodegradable composite nanomaterials for photothermal/chemodynamic synergistic therapy. *Int J Biol Macromol*. 2024;276(Pt 1):133583. doi:10.1016/j.ijbiomac.2024.133583
36. Bochani S, Zarepour A, Kalantari-Hesari A, et al. Injectable, antibacterial, and oxygen-releasing chitosan-based hydrogel for multimodal healing of bacteria-infected wounds. *J Mater Chem B*. 2023;11(33):8056–8068. doi:10.1039/d3tb01278f
37. Cui R, Li B, Liao C, Zhang S. Copper-mediated chemodynamic therapy with ultra-low copper consumption by doping cupric ion on cross-linked (R)-(+)-lipoic acid nanoparticles. *Regen Biomater*. 2023;10:rbad021. doi:10.1093/rb/rbad021
38. Li S, Ding H, Chang J, et al. Bimetallic oxide nanozyme-mediated depletion of glutathione to boost oxidative stress for combined nanocatalytic therapy. *J Colloid Interface Sci*. 2022;623:787–798. doi:10.1016/j.jcis.2022.05.059
39. Wang M, Zheng L, Ma S, Lin R, Li J, Yang S. Cuproptosis: emerging biomarkers and potential therapeutics in cancers. *Front Oncol*. 2023;13:1288504. doi:10.3389/fonc.2023.1288504